Shape transition with temperature of the pear-shaped nuclei in covariant density functional theory

W. Zhang (张炜)[1,2,3] and Y. F. Niu (牛一斐)[4,*]

[1]*Henan Key Laboratory of Ion-beam Bioengineering, Zhengzhou University, Zhengzhou 450052, China*
[2]*Key Laboratory of Precision Navigation and Technology, National Time Service Center, Chinese Academy of Sciences, Xi'an 710600, China*
[3]*Molecular Foundry, Lawrence Berkeley National Laboratory, Berkeley, California 94720, USA*
[4]*ELI-NP, Horia Hulubei National Institute for Physics and Nuclear Engineering, 30 Reactorului Street,*
RO-077125 Bucharest-Magurele, Romania

The shape evolutions of the pear-shaped nuclei ^{224}Ra and even-even $^{144-154}$Ba with temperature are investigated by the finite-temperature relativistic mean field theory with the treatment of pairing correlations by the BCS approach. The free energy surfaces as well as the bulk properties including deformations, pairing gaps, excitation energy, and specific heat for the global minimum are studied. For ^{224}Ra, three discontinuities found in the specific heat curve indicate the pairing transition at temperature 0.4 MeV and two shape transitions at temperatures 0.9 and 1.0 MeV, namely one from quadrupole-octupole deformed to quadrupole deformed, and the other from quadrupole deformed to spherical. Furthermore, the gaps at $N = 136$ and $Z = 88$ are responsible for stabilizing the octupole-deformed global minimum at low temperatures. Similar pairing transition at $T \sim 0.5$ MeV and shape transitions at $T = 0.5$–2.2 MeV are found for even-even $^{144-154}$Ba. The transition temperatures are roughly proportional to the corresponding deformations at the ground states.

I. INTRODUCTION

The shapes of atomic nuclei as well as the shape evolution and shape phase transition between the different shapes have been a hot topic for decades. At medium excitation energies in heavy-ion fusion, a completely equilibrated system is formed before the compound nucleus decays by particle or γ emission [1]. The canonical description of such a system is characterized by the temperature. When temperature rises, the shape deformations or superfluidity are expected to wash out [2]. Different from the shape evolution or shape phase transition by changing nucleon numbers, the shape changes may occur at certain critical temperatures in a single nucleus. Experimental information about nuclear shape changes can be obtained by means of the giant dipole resonance (GDR) built on excited states [3]. The theoretical models of GDR in excited nuclei can be found in Refs. [4–6] and references therein.

For the thermal description, the basic theory is developed in Refs. [7,8]. The shape transition at finite temperature was first studied in Ref. [9]. The finite-temperature Hartree-Fock approximation was developed [10,11] and the dependence of nuclear shape transition on the volume was studied by taking ^{24}Mg as an example [12]. The finite-temperature Hartree-Fock-Bogoliubov theory was formulated [13] and then applied to the pairing and shape transitions in rare-earth nuclei [14]. Using the finite-range density dependent Gogny force and a large configuration space within the framework of the finite-temperature Hartree-Fock-Bogoliubov (FTHFB) theory [2], varied nuclei, including well quadrupole-deformed nuclei, superdeformed nucleus, and octupole deformed nucleus, gradually collapse to the spherical shape at certain critical

temperatures in the range 1.3–2.7 MeV. Later the statistical shape fluctuation effects on representative nuclei ^{164}Er, ^{152}Dy, and ^{192}Hg in the quadrupole degree of freedom were taken into account with the Landau prescription based on the FTHFB theory [15]. It was found that the deformation parameters start to decrease earlier with temperature as compared with the plain FTHFB prediction, but shape transition signatures are washed out. The statistical fluctuations can be treated in the spirit of the Landau theory [15,16], or from a more fundamental point of view by using path integral techniques such as the static path approximation [17,18], the shell model Monte Carlo method [19], the particle number projected BCS method [20–22], or the shell-model-like approach [23]. The temperature also affects the effective mass and the neutron skin [24].

In the Ra-Th region, the octupole deformation is involved in shape evolution according to supportive experimental evidence [25–27]. A very low-lying negative-parity band, soon merging with the positive-parity one for $J > 5$, was observed in nuclei ^{224}Ra and ^{224}Th [25,26]. In 2013, based on the measured strong electric odd-multipole transitions connecting the low-lying parity doublets, ^{224}Ra was suggested to be a stable pear-shaped nucleus [27]. Since the nuclear Schiff moment (the electric-dipole distribution weighted by radius squared) and its resulting atomic electric dipole moment are signatures of time-reversal and parity violation, and they are expected to be amplified in octupole deformed nuclei, ^{224}Ra and its neighbor ^{225}Ra are of great importance for physics beyond the Standard Model [28].

It is interesting to explore the thermal properties of the octupole-deformed ^{224}Ra. In this work, we aim to investigate the shape evolution when the temperature rises for ^{224}Ra in the relativistic mean field (RMF) framework. The RMF theory, which has achieved great success in describing ground-state

*nyfster@gmail.com

properties of both spherical and deformed nuclei all over the nuclear chart [29–31], is also applied to study the shape evolution and phase transitions with temperature. The finite-temperature relativistic Hartree-Bogoliubov theory [32] and relativistic Hartree-Fock-Bogoliubov theory [33] for spherical nuclei are formulated, and used to study the pairing transitions in hot nuclei. The relativistic Hartree-BCS theory is applied to study the temperature dependence of shapes and pairing gaps for ^{166,170}Er and rare-earth nuclei [34,35]. A shape phase transition from prolate to spherical shapes is found at temperatures in the range 1.0–2.7 MeV. Taking into account the unbound nucleon states, the temperature dependence of the pairing gaps, nuclear deformation, radii, binding energies, and entropy are studied using Dirac-Hartree-Bogoliubov (DHB) calculations [36,37]. It is found that the nuclear deformation disappears at temperatures $T = 2.0$–4.0 MeV. When the temperature $T \geqslant 4$ MeV, the effects of the vapor phase that take into account the unbound nucleon states become important. Considering that different shape phase transition temperatures are found for varied nuclei in the covariant density functional framework, it is timely to discuss the transition temperatures for this typical octupole deformed nucleus ^{224}Ra with a novel point-coupling parameter set PC-PK1.

The paper will be organized as follows. The self-consistent finite-temperature RMF theory with BCS approach for axially deformed nuclei based on the point-coupling density functional will be briefly presented. After that, the free energy surface, the quadrupole and octupole deformations, the excitation energy, and the specific heat as functions of the temperature will be discussed. Finally the evolution of the single-particle spectra will be shown.

II. THEORETICAL FRAMEWORK

The starting point of the RMF theory is an effective Lagrangian density with zero-range point-coupling interaction between nucleons:

$$
\begin{aligned}
\mathcal{L} = {} & \bar{\psi}(i\gamma_\mu \partial^\mu - m)\psi - \frac{1}{2}\alpha_S(\bar{\psi}\psi)(\bar{\psi}\psi) \\
& - \frac{1}{2}\alpha_V(\bar{\psi}\gamma_\mu\psi)(\bar{\psi}\gamma^\mu\psi) - \frac{1}{2}\alpha_{TV}(\bar{\psi}\vec{\tau}\gamma_\mu\psi)\cdot(\bar{\psi}\vec{\tau}\gamma^\mu\psi) \\
& - \frac{1}{3}\beta_S(\bar{\psi}\psi)^3 - \frac{1}{4}\gamma_S(\bar{\psi}\psi)^4 - \frac{1}{4}\gamma_V[(\bar{\psi}\gamma_\mu\psi)(\bar{\psi}\gamma^\mu\psi)]^2 \\
& - \frac{1}{2}\delta_S\partial_\nu(\bar{\psi}\psi)\partial^\nu(\bar{\psi}\psi) - \frac{1}{2}\delta_V\partial_\nu(\bar{\psi}\gamma_\mu\psi)\partial^\nu(\bar{\psi}\gamma^\mu\psi) \\
& - \frac{1}{2}\delta_{TV}\partial_\nu(\bar{\psi}\vec{\tau}\gamma_\mu\psi)\cdot\partial^\nu(\bar{\psi}\vec{\tau}\gamma^\mu\psi) \\
& - \frac{1}{4}F^{\mu\nu}F_{\mu\nu} - e\bar{\psi}\gamma^\mu\frac{1-\tau_3}{2}\psi A_\mu,
\end{aligned}
\tag{1}
$$

which includes the free-nucleons term, the four-fermion point-coupling terms, the higher-order terms which are responsible for the effects of medium dependence, the gradient terms which are included to simulate the effects of finite range, and the electromagnetic interaction terms. The isovector-scalar channel is neglected. The Dirac spinor field of the nucleon is denoted by ψ, and the nucleon mass is m. $\vec{\tau}$ is the isospin Pauli matrix, and Γ generally denotes the 4×4 Dirac matrices

including $\gamma_\mu, \sigma_{\mu\nu}$ while greek indices μ and ν run over the Minkowski indices 0, 1, 2, and 3. α, β, γ, and δ with subscripts S (scalar), V (vector), TV (isovector) are coupling constants (adjustable parameters) in which α refers to the four-fermion term, β and γ respectively to the third- and fourth-order terms, and δ the derivative couplings.

Following the prescription in Ref. [13] where the BCS limit of finite-temperature Hartree-Fock Bogoliubov equations is derived, we obtain the finite-temperature RMF+BCS equation. The finite-temperature Dirac equation for single nucleons reads [38]

$$
[\gamma_\mu(i\partial^\mu - V^\mu) - (m + S)]\psi_k = 0,
\tag{2}
$$

where m is the nucleon mass. $\psi_k(\boldsymbol{r})$ denotes the Dirac spinor field of a nucleon. The scalar $S(\boldsymbol{r})$ and vector $V^\mu(\boldsymbol{r})$ potentials are

$$
S(\boldsymbol{r}) = \alpha_S\rho_S + \beta_S\rho_S^2 + \gamma_S\rho_S^3 + \delta_S\triangle\rho_S,
\tag{3}
$$

$$
\begin{aligned}
V^\mu(\boldsymbol{r}) = {} & \alpha_V j_V^\mu + \gamma_V\left(j_V^\mu\right)^3 + \delta_V\triangle j_V^\mu \\
& + \tau_3\alpha_{TV}\vec{j}_{TV}^\mu + \tau_3\delta_{TV}\triangle\vec{j}_{TV}^\mu + eA^\mu
\end{aligned}
\tag{4}
$$

respectively. The isoscalar density ρ_S, isoscalar current j_V^μ and isovector current $\vec{j}_{TV}^\mu$ are represented by

$$
\rho_S(\boldsymbol{r}) = \sum_k \bar{\psi}_k(\boldsymbol{r})\psi_k(\boldsymbol{r})\left[v_k^2(1 - 2f_k) + f_k\right],
\tag{5}
$$

$$
j_V^\mu(\boldsymbol{r}) = \sum_k \bar{\psi}_k(\boldsymbol{r})\gamma^\mu\psi_k(\boldsymbol{r})\left[v_k^2(1 - 2f_k) + f_k\right],
\tag{6}
$$

$$
\vec{j}_{TV}^\mu(\boldsymbol{r}) = \sum_k \bar{\psi}_k(\boldsymbol{r})\vec{\tau}\gamma^\mu\psi_k(\boldsymbol{r})\left[v_k^2(1 - 2f_k) + f_k\right].
\tag{7}
$$

where the thermal occupation probability of quasiparticle states f_k is directly related to the temperature T by $f_k = 1/(1 + e^{E_k/k_B T})$. E_k is the quasiparticle energy for single particle (s.p.) state k, $E_k = [(\epsilon_k - \lambda_q)^2 + (\Delta_k)^2]^{\frac{1}{2}}$. In Eqs. (5)–(7), the BCS occupation probabilities v_k^2 and associated $u_k^2 = 1 - v_k^2$ are obtained by

$$
v_k^2 = \frac{1}{2}\left(1 - \frac{\epsilon_k - \lambda_q}{E_k}\right),
\tag{8}
$$

$$
u_k^2 = \frac{1}{2}\left(1 + \frac{\epsilon_k - \lambda_q}{E_k}\right).
\tag{9}
$$

Δ_k is the pairing gap parameter, which satisfies the gap equation at finite temperature.

$$
\Delta_k = -\frac{1}{2}\sum_{k'>0} V_{k\bar{k}k'\bar{k}'}^{pp}\frac{\Delta_{k'}}{E_{k'}}(1 - 2f_{k'}).
\tag{10}
$$

The particle number N_q is restricted by $N_q = 2\sum_{k>0}[v_k^2(1 - 2f_k) + f_k]$.

Here we take the δ pairing force $V(\boldsymbol{r}) = V_q\delta(\boldsymbol{r})$, where V_q is the pairing strength parameter for neutrons or protons. A smooth energy-dependent cutoff weight g_k having the form $\{1 + \exp[(\epsilon_k - \lambda_q - E_c)/(E_c/10)]\}^{-1}$, where E_c is the cutoff parameter, is introduced to simulate the effect of finite range in the evaluation of local pair density. The cutoff parameter is determined by an approximate condition
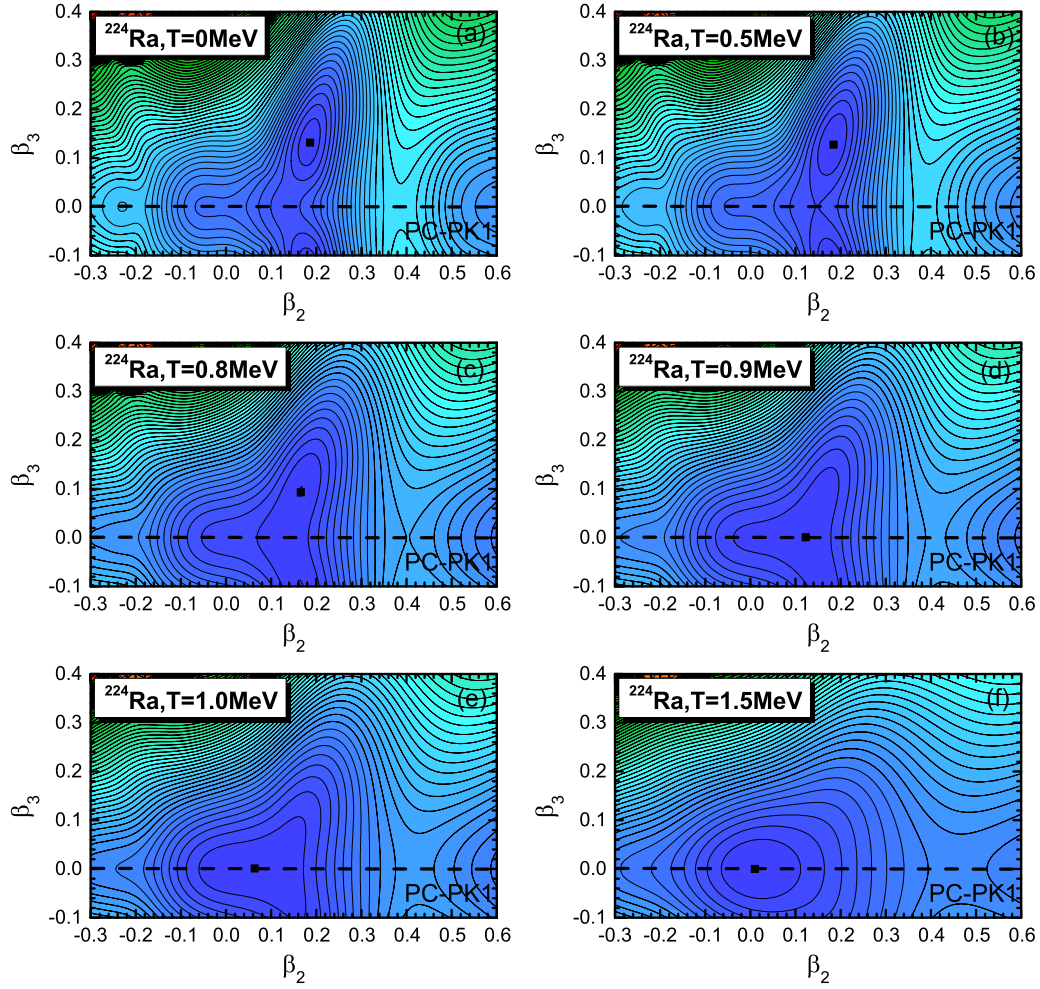
FIG. 1. The free energy surfaces in the (β_2, β_3) plane at temperatures $T = 0$ (a), 0.5 (b), 0.8 (c), 0.9 (d), 1.0 (e), and 1.5 (f) MeV for ^{224}Ra obtained by the finite-temperature RMF+BCS calculations using the PC-PK1 energy density functional. The global minima are indicated by the solid squares. The energy separation between contour lines is 0.5 MeV.

$\sum_k 2g_k = N_q + 1.65N_q^{2/3}$ related to the particle number N_q, where q can refer to neutron or proton [39].

The internal binding energies E at different axial-symmetric shapes can be obtained by applying constraints with quadrupole deformation β_2 and octupole deformation β_3 together. In the mean-field level, the binding energy with a given deformation β_2 can be obtained by minimizing

$$\langle H' \rangle = \langle H \rangle + \frac{1}{2}C(\langle \hat{Q}_2 \rangle - \mu_2)^2, \qquad (11)$$

where C is a spring constant, $\mu_2 = \frac{3AR^2}{4\pi}\beta_2$ is the given quadrupole moment, and $\langle \hat{Q}_2 \rangle$ is the expectation value of qudrupole moment operator $\hat{Q}_2 = 2r^2 P_2(\cos\theta)$. The octupole moment constraint can also be applied similarly with $\hat{Q}_3 = 2r^3 P_3(\cos\theta)$ and $\mu_3 = \frac{3AR^3}{4\pi}\beta_3$.

The free energy for the system is $F = E - TS$ where the entropy S is evaluated from

$$S = -k_B \sum_k [f_k \ln f_k + (1 - f_k)\ln(1 - f_k)]. \qquad (12)$$

For convenience, the temperature used is $k_B T$ in units of MeV and the entropy used is S/k_B and is unitless. The free energy surface in the (β_2, β_3) plane is obtained by plotting the free energy $E(\beta_2, \beta_3) - TS(\beta_2, \beta_3)$ on a mesh with equidistant β_2 and β_3.

The specific heat is defined by the relation

$$C_v = \partial E^*/\partial T, \qquad (13)$$

where $E^*(T) = E(T) - E(T = 0)$ is the internal excitation energy, and $E(T)$ is the internal binding energy for the global minimum state in the free energy surface at certain temperature T.

III. RESULTS AND DISCUSSION

The point-coupling density functional parameter set PC-PK1 is used in our calculation due to its success in the description of finite nuclei for both the ground state and low-lying excited states [40]. The pairing correlations are taken into account by the BCS method with a δ pairing force. The value of the pairing strength for neutrons (protons) V_q is taken from Ref. [40], that is, -349.5 (-330.0) MeV fm^3. A set of axial harmonic oscillator basis functions with 20 major shells is used.
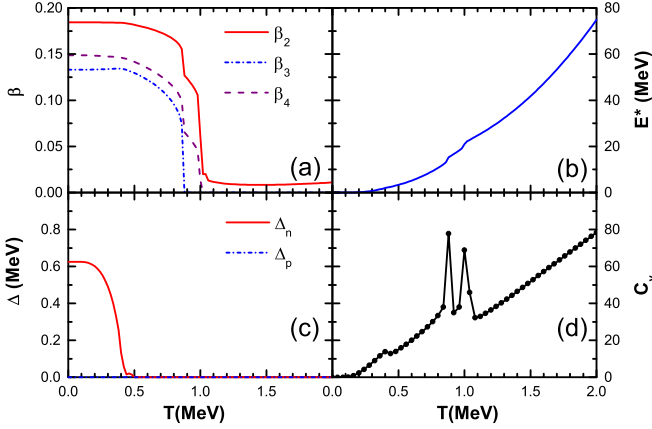
FIG. 2. The global minima deformations β_2, β_3, β_4 (a), excitation energies E^* (in MeV) (b), pairing gaps Δ_n, Δ_p (in MeV) (c), and the specific heat C_v (d) as functions of temperature (in MeV) for ^{224}Ra, obtained by the finite-temperature RMF+BCS calculations using the PC-PK1 energy density functional.

FIG. 3. Neutron (a) and proton (b) single-particle levels as a function of temperature (in MeV) for the nucleus ^{224}Ra, obtained by constrained RMF+BCS calculations using the PC-PK1 energy density functional. The dash-dot lines denote the corresponding Fermi surfaces. The levels near the Fermi surface are labeled by Nilsson notations $\Omega\pi[Nn_zm_l]$ of the first leading component.

The free energies in the (β_2,β_3) plane at temperatures $T = 0$, 0.5, 0.8, 0.9, 1.0, and 1.5 MeV for ^{224}Ra are plotted in Fig. 1. For zero temperature in Fig. 1(a), the free energy for the global minimum at zero temperature, which equals the internal binding energy for the ground state, is close to the experimental binding energy for ^{224}Ra within 0.1%. The corresponding deformations $\beta_2 = 0.184$, $\beta_3 = 0.133$ are slightly bigger than the experimental data $\beta_2 = 0.154$, $\beta_3 = 0.097$ in Ref. [27]. Such a result is also consistent with other theoretical calculations, e.g., $\beta_2 = 0.179$, $\beta_3 = 0.125$ for parameter set PC-PK1 in Ref. [41] and $\beta_2 = 0.177$, $\beta_3 = 0.125$ for parameter set DD-PC1, $\beta_2 = 0.178$, $\beta_3 = 0.124$ for parameter set NL3* in Ref. [42]. The saddle point is purely quadrupole deformed, about 1.1 MeV higher than the global minimum. When the temperature rises up to 0.5 MeV, the deformations of the global minimum change little. In the temperature range $0.5 \leqslant T \leqslant 1.0$ MeV, the energy surfaces change dramatically. The energy difference between the saddle point and global minimum gradually decreases, and finally drops to zero. At $T \sim 0.9$ MeV, the saddle point and global minimum merge together at $\beta_2 = 0.12$ and $\beta_3 = 0$, and the shape phase transition from octupole deformed to quadrupole deformed occurs. For $0.8 \leqslant T \leqslant 1.0$ MeV, a relatively soft area near the global minimum is composed; e.g., at $T = 0.9$ MeV the states with $-0.04 \leqslant \beta_2 \leqslant 0.18$, $\beta_3 = 0$, or $\beta_2 = 0.19$, $\beta_3 = 0.14$ are no more than 0.5 MeV higher than the global minimum. At $T \sim 1.0$ MeV, the global minimum moves to a spheroidal shape at $\beta_2 = 0.02$ and $\beta_3 = 0$, and the nucleus has another shape phase transition from quadrupole deformed to spherical shape. When the temperature continues rising above 1.5 MeV, the energy surfaces evolves little with a single minimum near spherical state.

To see the properties of the nuclei as functions of temperatures in more detail, the evolution of deformations, pairing gaps, the excitation energy as well as the specific heat for ^{224}Ra using the PC-PK1 energy density functional are shown in Fig. 2. In Fig. 2(a), the global minimum deformations are almost constant for $T \leqslant 0.5$ MeV. At temperatures 0.9
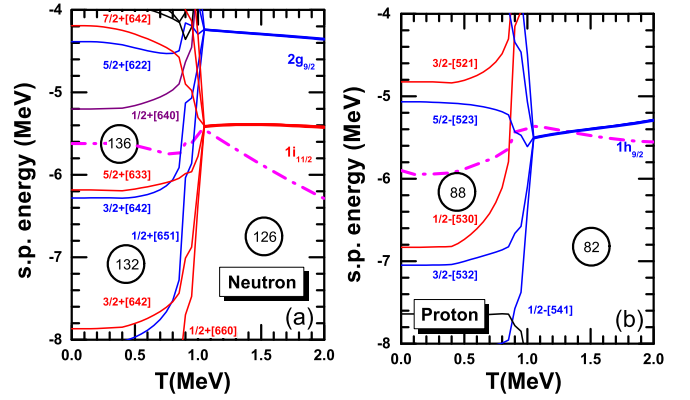
and 1.0 MeV, the quadrupole and octupole deformations quickly drop to zero respectively. The hexadecapole deformation behaves similar to the quadrupole deformation. So the nucleus first goes through a shape transition from octupole to quadrupole, and then another shape transition from quadrupole and hexadecapole deformed to spherical. The vanishing of octupole deformation also interplays with quadrupole and hexadecapole deformations, which causes sudden decreases in the quadrupole and hexadecaple deformations. In Fig. 2(c), the neutron pairing gap at zero temperature is $\Delta_n(0) = 0.63$ MeV, and it decreases to zero at a critical temperature $T_c = 0.40$ MeV, which shows a pairing phase transition. The critical temperature for the pairing phase transition in the case of deformed nuclei basically follows the rule $T_c = 0.6\Delta_n(0)$, which was discovered for spherical nuclei [32]. Since the global minimum deformation for $T \leqslant T_c$ changes little, as seen in Fig. 2(a), the single-particle levels, which are sensitive to the deformation but insensitive to the temperature, are barely altered for $T \leqslant T_c$. It is speculated that the rule $T_c = 0.6\Delta(0)$ is kept for a fixed single-particle level structure, no matter whether the nucleus prefers a spherical, oblate, or prolate minimum. Such a rule may not hold for a gradually changing minimum or oscillating minimum. In Fig. 2(c), the proton pairing gap is zero. Such a proton pairing collapse is caused by a larger gap near the Fermi surface and weaker pairing strength compared with the neutron counterpart. At zero temperature, the proton shell gap near the Fermi surface is about 1.7 MeV while the corresponding neutron shell gap is 1 MeV (cf. Fig. 3). Moreover, for the PC-PK1 parameter set, the proton pairing strength -330 MeV fm^3 is about 5.6% weaker than the corresponding neutron pairing strength -349.5 MeV fm^3. Compared with Ref. [2], where the proton pairing energy is a nonzero value -2 MeV, our pairing strength is in general smaller, which we could see by comparing the neutron pairing energy. In Ref. [2] the neutron pairing energy at zero temperature is -5 MeV, while it is -3.2 MeV in our calculation.
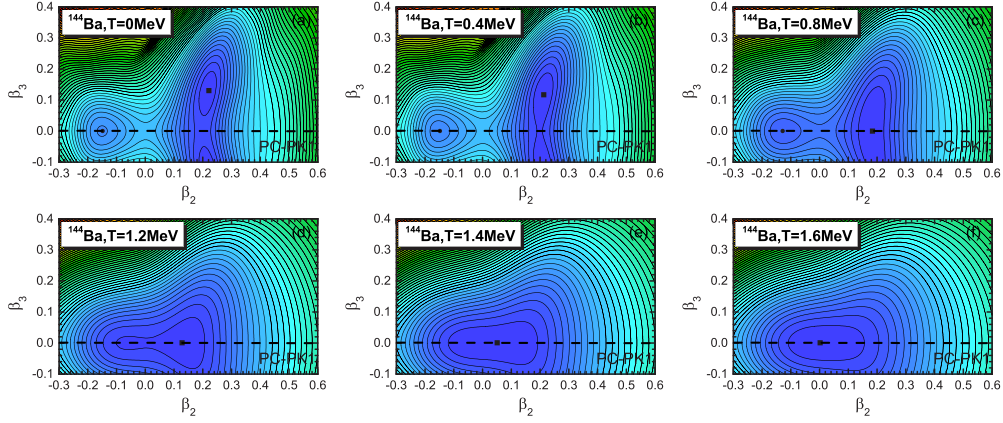
FIG. 4. Same as Fig. 1, but at temperatures $T = 0$ (a), 0.4 (b), 0.8 (c), 1.2 (d), 1.4 (e), and 1.6 (f) MeV for ^{144}Ba.

For the relative excitation energy E^* in Fig. 2(b), one inappreciable kink at low temperatures and two noticeable kinks at medium temperatures can be found. Its derivative, namely the specific heat, is plotted in Fig. 2(d). Three discontinuities in Fig. 2(d) correspond to three kinks in Fig. 2(b). It is well known that the appearance of discontinuities in this quantity is customarily interpreted as a signature of transitions. The discontinuity at $T_c = 0.4$ MeV indicates the transition from the superfluid to the normal phase. Two peaks at 0.9 and 1.0 MeV indicate two shape transitions, namely one from quadrupole-octupole deformed to quadrupole deformed (octupole transition for short), and the other from quadrupole deformed to spherical (quadrupole transition for short). However, in experiments the specific heat usually exhibits a more smooth behavior than compared to the sharp discontinuity obtained here. This is attributed to the finite size of the nucleus and, therefore, a realistic description of statistical and quantal fluctuations. The two adjacent shape transitions would be smeared into one. In the finite-temperature HFB theory [2], ^{224}Ra experiences similar transitions: first a pairing transition at $T = 0.5$ MeV, and

after that the octupole deformation continuously decreases and finally becomes zero at $T = 1.3$ MeV together with abrupt changes in quadrupole and hexadecapole deformations [2]. The signature of such transition at $T = 1.3$ MeV can also be found in the corresponding specific heat. It is found that for ^{224}Ra the proton single-particle gap of $Z = 88$ at the deformed equilibrium in the RMF calculation is relatively smaller than that of the corresponding Gogny D1S calculation [43]. With a smaller shell gap, the shape transition can be achieved at a lower temperature, which is 1.0 MeV in the RMF calculation compared to 1.3 MeV in the Gogny calculation [2]. Such a smaller shell gap near $Z = 88$ is related to the artificial shell closure $Z = 92$ (above $1h_{9/2}$) in the spherical state, which is commonly found in RMF calculations, and can be cured by the presence of the degree of freedom associated with the Lorentz tensor ρ field [44,45].

In Fig. 3, we plot the single-particle (s.p.) levels of neutrons and protons at the global minimum as a function of temperature for ^{224}Ra. Normally the octupole interaction couples the pairs of orbitals with $\Delta N = 1$, $\Delta l = 3$, and $\Delta j = 3$ near the Fermi surface. The regions of nuclei with strong octupole correlations
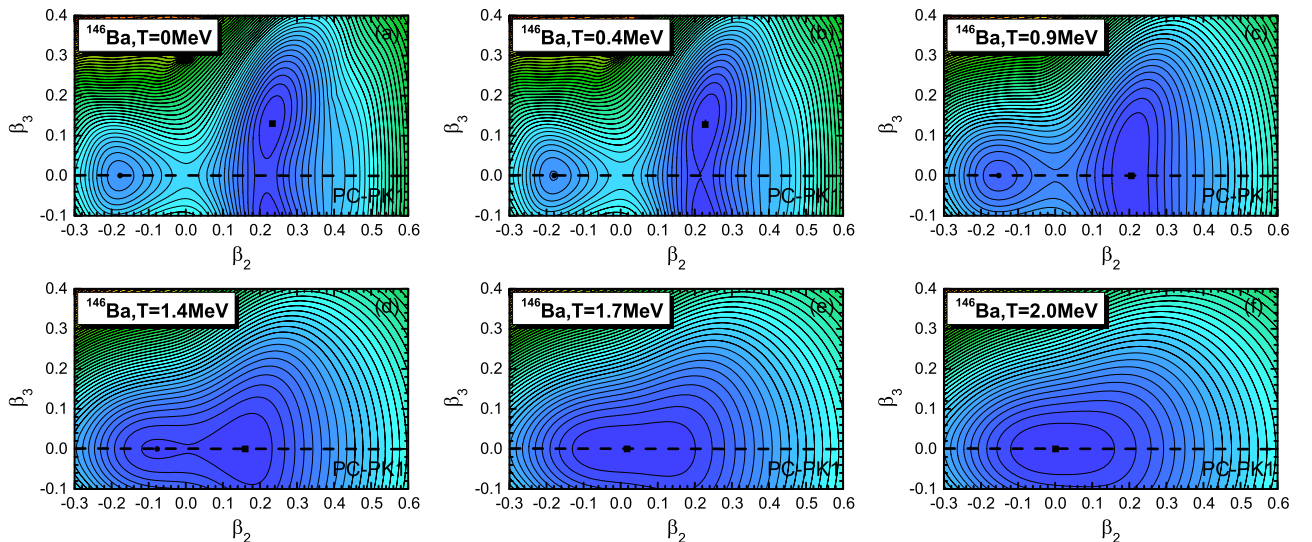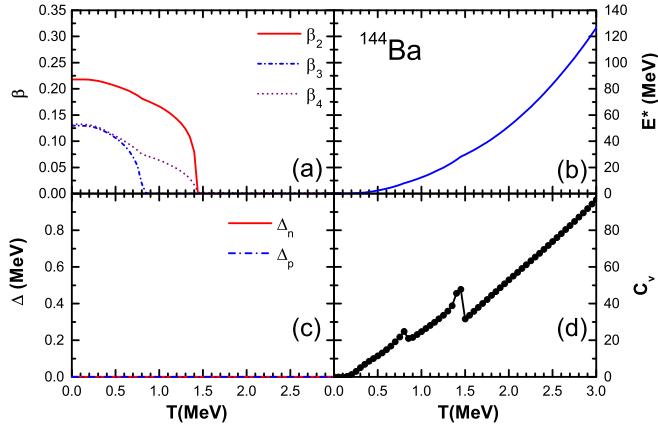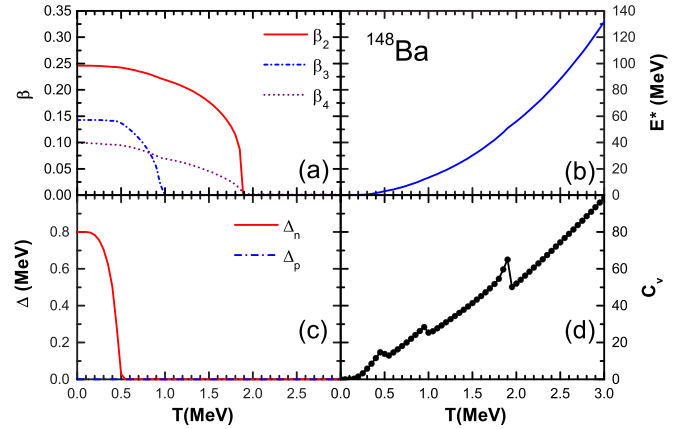

FIG. 5. Same as Fig. 1, but at temperatures $T = 0$ (a), 0.4 (b), 0.9 (c), 1.4 (d), 1.7 (e), 2.0 (f) MeV for ^{146}Ba.

FIG. 6. Same as Fig. 2, but for ^{144}Ba.
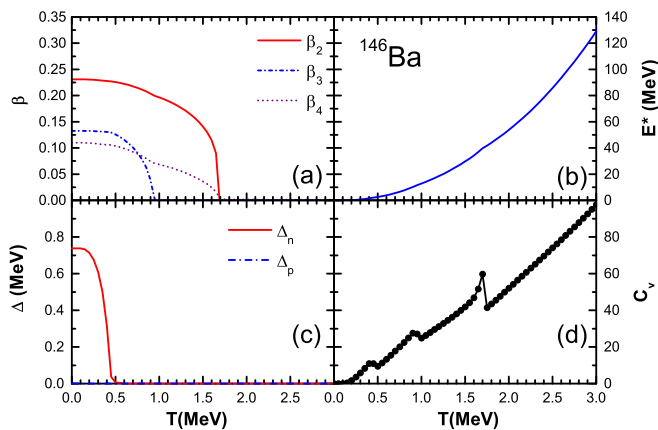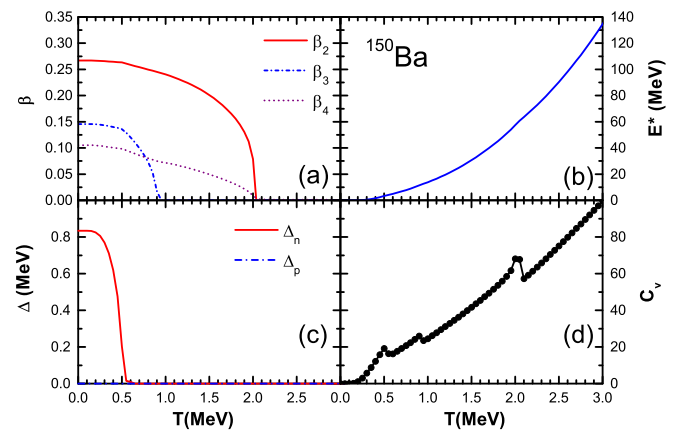

FIG. 8. Same as Fig. 2, but for ^{148}Ba.

correspond to either the proton or neutron numbers being close to 34 ($1g_{9/2} \leftrightarrow 2p_{3/2}$ coupling), 56 ($1h_{11/2} \leftrightarrow 2d_{5/2}$ coupling), 88 ($1i_{13/2} \leftrightarrow 2f_{7/2}$ coupling), and 134 ($1j_{15/2} \leftrightarrow 2g_{9/2}$ coupling) [46]. A gap at $N = 136$ together with another gap at $N = 132$ for $T < 1$ MeV and a big gap at $N = 126$ for $T > 1$ MeV can be found in Fig. 3(a), while a gap at $Z = 88$ for $T < 1$ MeV and a big gap at $Z = 82$ for $T > 1$ MeV can be found in Fig. 3(b). Since the s.p. levels are sensitive to slight deformations, for the spheroidal global minimum when $T > 1$ MeV the s.p. levels constituting $\nu 2g_{9/2}$, $\nu 1i_{11/2}$, and $\pi 1h_{9/2}$ do not degenerate rigorously. The gaps at $N = 136$ and $Z = 88$ are responsible to the octupole-deformed global minimum at low temperatures. With temperature increasing, more and more nucleons are thermally excited to s.p. levels above the shell gaps, so the shell effect becomes weaker and disappears eventually. As a result, the shape of the nucleus becomes spherical at high temperature.

Additionally, we focus on neutron-rich ^{144}Ba and ^{146}Ba where direct experimental evidence of octupole deformation was found recently [47,48]. The free energies in the (β_2, β_3) plane at different temperatures for ^{144,146}Ba are plotted in Figs. 4 and 5 respectively. At zero temperature in Figs. 4(a) and 5(a), the octupole-deformed ground states of both ^{144}Ba and ^{146}Ba are about 0.6 MeV lower than the quadrupole-deformed

saddle points. The calculated ground state quadrupole and octupole deformations are in good agreement with the experimental data. For ^{144}Ba, the experimental data are $\beta_2 = 0.18$, $\beta_3 = 0.11$–0.21 [47] while the calculated ones are $\beta_2 = 0.22$, $\beta_3 = 0.13$. With increasing temperature before the octupole transition temperature in Figs. 4(b) and 5(b), the energy differences between the global minimum and the saddle points become shallower. At the octupole transition temperature in Figs. 4(c) and 5(c), the energy surface in the β_3 direction is softer than in the β_2 direction. Note the oblate minima continuously become shallower in Figs. 4(b), 4(c) and 5(b), 5(c). At temperature higher than the octupole transition temperature in Figs. 4(d) and 5(d), a soft deformation area around the spherical state is developed with the disappearance of the oblate minima. The transition from quadrupole deformed to spherical phase occurs in Figs. 4(e) and 5(e), while the spherical states are kept as the global minima in Figs. 4(f) and 5(f). It should be noted that the free energy surfaces near or at the transitions are very similar for ^{144,146}Ba, but the transition temperatures vary; e.g., in Figs. 4(e) and 5(e) the quadrupole transition temperatures for ^{144,146}Ba are 1.4 and 1.7 MeV respectively.

Moreover, even-even $^{144-154}$Ba isotopes are studied using the same method, and their properties are shown in

FIG. 7. Same as Fig. 2, but for ^{146}Ba.

FIG. 9. Same as Fig. 2, but for ^{150}Ba.
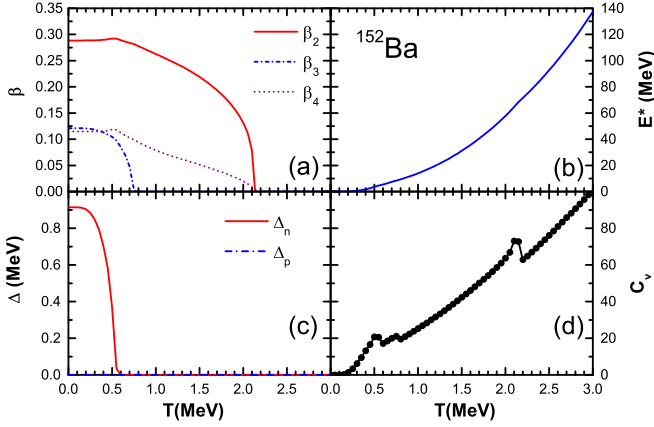
FIG. 10. Same as Fig. 2, but for ^{152}Ba.

Figs. 6–11. The quadrupole deformation for $^{144-154}$Ba ground states is increasing since the neutron number is approaching the middle of a shell between the closures 82 and 126, while the corresponding octupole deformation is decreasing as the neutron number is departing from 88 where the strong octupole correlation is believed to occur [46]. The results are also consistent with calculations of parameter sets PK1 [49], DD-PC1 [42], and NL3* [42]. For each isotope, when the temperature rises, similar to ^{224}Ra, the global minima quadrupole and octupole deformations evolve with the temperature similarly, where they change slowly for temperatures below the transition temperature and then quickly drop to zero approaching the transition temperature. Note the quadrupole and octupole transition temperatures for each isotope are separated. The hexadecapole deformation drops little at the octupole transition temperature and vanishes at the quadrupole transition temperature. Concerning the transition temperatures as functions of neutron number, it is observed that the quadrupole transition temperature increases when the nuclei become heavier while the octupole transition temperature remains nearly constant and finally decreases in Figs. 6(a)–11(a). For clarity, the quadrupole and octupole transition temperatures together with the quadrupole and octupole deformations at the ground states are listed in Table I. It is
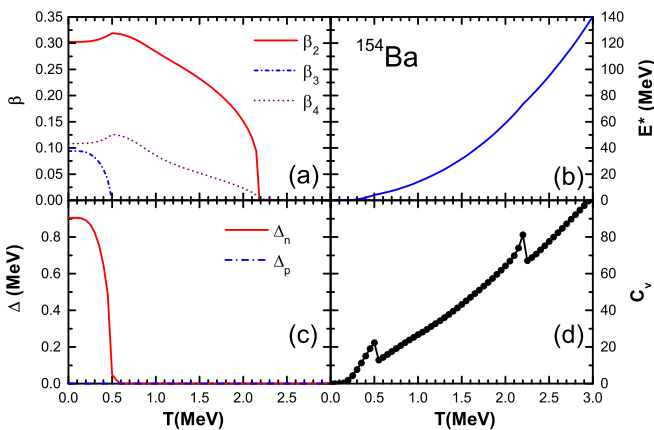

FIG. 11. Same as Fig. 2, but for ^{154}Ba.

TABLE I. The quadrupole and octupole transition temperatures T_2 and T_3 (in MeV), together with the quadrupole and octupole deformations β_2 and β_3 at the ground states for even-even $^{144-154}$Ba, obtained by constrained RMF+BCS calculations using the PC-PK1 energy density functional.

Nucleus	β_2	T_2 (MeV)	β_3	T_3 (MeV)
^{144}Ba	0.22	1.45	0.13	0.85
^{146}Ba	0.23	1.70	0.13	0.95
^{148}Ba	0.25	1.90	0.14	0.95
^{150}Ba	0.27	2.05	0.15	0.95
^{152}Ba	0.29	2.15	0.12	0.75
^{154}Ba	0.30	2.20	0.09	0.50

found that, for even-even $^{144-154}$Ba isotopes, the quadrupole and octupole transition temperatures are roughly linearly proportional to the quadrupole and octupole deformations at the ground states. Similar to the above discussion on ^{224}Ra, $^{144-154}$Ba may suffer from the neutron artificial shell $N = 92$, getting lower transition temperatures.

For the pairing correlations in Figs. 6(c)–11(c), only neutron pairing gaps of around 0.8 MeV survive except for pairing collapse in ^{144}Ba. All critical temperatures for pairing phase transitions follow the rule $T_c = 0.6\Delta_n(0)$. For the relative excitation energies in Figs. 6(b)–11(b), some inappreciable kinks corresponding to the pairing and shape transitions can be found. These kinks are manifested more clearly in the specific heat in Figs. 6(d)–11(d), where three discontinuities corresponding to one pairing transition and two shape transition temperatures are found except for ^{144,154}Ba. For ^{144}Ba, the pairing transition is absent as a direct result of pairing collapse. For ^{154}Ba, the pairing transition coincides with the octupole shape transition. The discontinuities of the specific heat in Figs. 6(d)–11(d) are consistent with transition temperatures in Figs. 6(a)–11(a).

IV. SUMMARY

In summary, the finite-temperature deformed RMF+BCS theory based on the relativistic point-coupling density functional is applied to the shape evolution study of ^{224}Ra and even-even $^{144-154}$Ba with temperature. The free energy surfaces as well as the bulk properties including deformations, pairing gaps, excitation energy, and specific heat for the global minimum are investigated. For ^{224}Ra, three discontinuities are found in the specific heat curve, indicating the pairing transition at temperature 0.4 MeV and two shape transitions at temperatures 0.9 and 1.0 MeV, namely one from quadrupole-octupole deformed to quadrupole deformed, and the other from quadrupole deformed to spherical. Furthermore, the single -particle levels as functions of the temperature are analyzed. The gaps at $N = 136$ and $Z = 88$ are responsible for stabilizing the octupole-deformed global minimum at low temperatures. With rising temperature, the shell effects disappear. Similar pairing transition at $T \sim 0.5$ MeV and shape transitions at $T = 0.5 \sim 2.2$ MeV are found for even-even $^{144-154}$Ba. Roughly there is a simple proportional relation between the quadrupole and octupole transition temperatures

and the quadrupole and octupole deformations at the ground states. The realistic description of statistical and quantal fluctuations is under consideration.

[1] J. L. Egido and P. Ring, J. Phys. G **19**, 1 (1993).
[2] J. L. Egido, L. M. Robledo, and V. Martin, Phys. Rev. Lett. **85**, 26 (2000).
[3] A. Schiller and M. Thoennessen, At. Data Nucl. Data Tables **93**, 549 (2007).
[4] P. Ring, L. M. Robledo, J. L. Egido, and M. Faber, Nucl. Phys. A **419**, 261 (1984).
[5] Y. F. Niu, N. Paar, D. Vretenar, and J. Meng, Phys. Lett. B **681**, 315 (2009).
[6] D. R. Chakrabarty, N. Dinh Dang, and V. M. Datar, Eur. Phys. J. A **52**, 143 (2016).
[7] C. Bloch and C. Dedominicis, Nucl. Phys. **7**, 459 (1958).
[8] G. Sauer, H. Chandra, and U. Mosel, Nucl. Phys. A **264**, 221 (1976).
[9] H. C. Lee and S. Das Gupta, Phys. Rev. C **19**, 2369 (1979).
[10] M. Brack and P. Quentin, Phys. Lett. B **52**, 159 (1974); Phys. Scr. **A10**, 163 (1974).
[11] P. Quentin and H. Flocard, Annu. Rev. Nucl. Part. Sci. **28**, 523 (1978).
[12] G. D. Yen and H. G. Miller, Phys. Rev. C **50**, 807 (1994).
[13] A. L. Goodman, Nucl. Phys. A **352**, 30 (1981).
[14] A. L. Goodman, Phys. Rev. C **34**, 1942 (1986).
[15] V. Martin, J. L. Egido, and L. M. Robledo, Phys. Rev. C **68**, 034327 (2003).
[16] S. Levit and Y. Alhassid, Nucl. Phys. A **413**, 439 (1984).
[17] Y. Alhassid and J. Zingman, Phys. Rev. C **30**, 684 (1984).
[18] R. Rossignoli and P. Ring, Ann. Phys. (NY) **235**, 350 (1994).
[19] G. H. Lang, C. W. Johnson, S. E. Koonin, and W. E. Ormand, Phys. Rev. C **48**, 1518 (1993).
[20] N. D. Dang, P. Ring, and R. Rossignoli, Phys. Rev. C **47**, 606 (1993).
[21] N. D. Dang, Phys. Rev. C **76**, 064320 (2007).
[22] D. Gambacurta, D. Lacroix, and N. Sandulescu, Phys. Rev. C **88**, 034324 (2013).
[23] L. Liu, Z. H. Zhang, and P. W. Zhao, Phys. Rev. C **92**, 044304 (2015).
[24] E. Yüksel, E. Khan, K. Bozkurt, and G. Colò, Eur. Phys. J. A **50**, 160 (2014).
[25] P. G. Bizzeti, in *Symmetries in Physics*, edited by A. Vitturi and R. Casten (World Scientific, Singapore, 2003), p. 262.
[26] P. G. Bizzeti and A. M. Bizzeti-Sona, in *Nuclear Theory 24*, edited by S. Dimitrova (Heron Press, Sofia, 2005), p. 311.

[27] L. P. Gaffney *et al.*, Nature (London) **497**, 199 (2013).
[28] J. Engel, M. J. Ramsey-Musolf, and U. van Kolck, Prog. Part. Nucl. Phys. **71**, 21 (2013).
[29] P. Ring, Prog. Part. Nucl. Phys. **37**, 193 (1996).
[30] D. Vretenar, A. V. Afanasjev, G. A. Lalazissis, and P. Ring, Phys. Rep. **409**, 101 (2005).
[31] J. Meng, H. Toki, S.-G. Zhou, S. Q. Zhang, W. H. Long, and L. S. Geng, Prog. Part. Nucl. Phys. **57**, 470 (2006).
[32] Y. F. Niu, Z. M. Niu, N. Paar, D. Vretenar, G. H. Wang, J. S. Bai, and J. Meng, Phys. Rev. C **88**, 034308 (2013).
[33] J. J. Li, J. Margueron, W. H. Long, and N. Van Giai, Phys. Rev. C **92**, 014302 (2015).
[34] B. K. Agrawal, Tapas Sil, J. N. De, and S. K. Samaddar, Phys. Rev. C **62**, 044307 (2000).
[35] B. K. Agrawal, Tapas Sil, S. K. Samaddar, and J. N. De, Phys. Rev. C **63**, 024002 (2001).
[36] P. Bonche, S. Levit, and D. Vautherin, Nucl. Phys. A **427**, 278 (1984); **436**, 265 (1985).
[37] R. Lisboa, M. Malheiro, and B. V. Carlson, Phys. Rev. C **93**, 024321 (2016).
[38] W. Zhang and Y. F. Niu, Chin. Phys. C **41**, 094102 (2017).
[39] M. Bender, K. Rutz, P.-G. Reinhard, and J. A. Maruhn, Eur. Phys. J. A **8**, 59 (2000).
[40] P. W. Zhao, Z. P. Li, J. M. Yao, and J. Meng, Phys. Rev. C **82**, 054319 (2010).
[41] J. M. Yao, E. F. Zhou, and Z. P. Li, Phys. Rev. C **92**, 041304(R) (2015).
[42] S. E. Agbemava, A. V. Afanasjev, and P. Ring, Phys. Rev. C **93**, 044304 (2016).
[43] L. M. Robledo, M. Baldo, P. Schuck, and X. Viñas, Phys. Rev. C **81**, 034315 (2010).
[44] W. H. Long, H. Sagawa, N. V. Giai, and J. Meng, Phys. Rev. C **76**, 034314 (2007).
[45] J. Meng, *Relativistic Density Functional for Nuclear Structure* (World Scientific, Singapore, 2016), p. 159.
[46] P. A. Butler and W. Nazarewicz, Rev. Mod. Phys. **68**, 349 (1996).
[47] B. Bucher *et al.*, Phys. Rev. Lett. **116**, 112503 (2016).
[48] B. Bucher *et al.*, Phys. Rev. Lett. **118**, 152504 (2017).
[49] W. Zhang, Z. P. Li, and S. Q. Zhang, Chin. Phys. C **34**, 1094 (2010).